

## Subnanomolar Inhibitor of Cytochrome *bc*<sub>1</sub> Complex Designed by Optimizing Interaction with Conformationally Flexible Residues

Pei-Liang Zhao,<sup>†</sup> Le Wang,<sup>‡</sup> Xiao-Lei Zhu,<sup>†</sup> Xiaoqin Huang,<sup>§</sup> Chang-Guo Zhan,<sup>\*§</sup>  
Jia-Wei Wu,<sup>\*‡</sup> and Guang-Fu Yang<sup>\*†</sup>

Key Laboratory of Pesticide & Chemical Biology, College of Chemistry, Ministry of Education,  
Central China Normal University, Wuhan 430079, P.R. China, MOE Key Laboratory of  
Bioinformatics, Department of Biological Sciences and Biotechnology, Tsinghua University,  
Beijing 100084, P.R. China, and Department of Pharmaceutical Sciences, College of Pharmacy,  
University of Kentucky, 725 Rose Street, Lexington, Kentucky 40536

Received July 12, 2009; E-mail: gfyang@mail.ccnu.edu.cn; jiaweiwu@mail.tsinghua.edu.cn; zhan@uky.edu

**Abstract:** Cytochrome *bc*<sub>1</sub> complex (EC 1.10.2.2, *bc*<sub>1</sub>), an essential component of the cellular respiratory chain and the photosynthetic apparatus in photosynthetic bacteria, has been identified as a promising target for new drugs and agricultural fungicides. X-ray diffraction structures of the free *bc*<sub>1</sub> complex and its complexes with various inhibitors revealed that the phenyl group of Phe274 in the binding pocket exhibited significant conformational flexibility upon different inhibitors binding to optimize respective  $\pi$ - $\pi$  interactions, whereas the side chains of other hydrophobic residues showed conformational stability. Therefore, in the present study, a strategy of optimizing the  $\pi$ - $\pi$  interaction with conformationally flexible residues was proposed to design and discover new *bc*<sub>1</sub> inhibitors with a higher potency. Eight new compounds were designed and synthesized, among which compound **5c**, with a *K*<sub>i</sub> value of 570 pM, was identified as the most promising drug or fungicide candidate, significantly more potent than the commercially available *bc*<sub>1</sub> inhibitors, including azoxystrobin (AZ), kresoxim-methyl (KM), and pyraclostrobin (PY). To our knowledge, this is the first *bc*<sub>1</sub> inhibitor discovered from structure-based design with a potency of subnanomolar *K*<sub>i</sub> value. For all of the compounds synthesized and assayed, the calculated binding free energies correlated reasonably well with the binding free energies derived from the experimental *K*<sub>i</sub> values, with a correlation coefficient of  $r^2 = 0.89$ . The further inhibitory kinetics studies revealed that **5c** is a noncompetitive inhibitor with respect to substrate cytochrome *c*, but it is a competitive inhibitor with respect to substrate ubiquinol. Due to its subnanomolar *K*<sub>i</sub> potency and slow dissociation rate constant ( $k_{-0} = 0.00358 \text{ s}^{-1}$ ), **5c** could be used as a specific probe for further elucidation of the mechanism of *bc*<sub>1</sub> function and as a new lead compound for future drug discovery.

### Introduction

Understanding drug–receptor interactions is the molecular basis of designing new compounds with higher potency.<sup>1</sup> In fact, the interaction between drug and receptor is the interaction between the bioactive conformation of a drug molecule and the residues in the binding pocket of its receptor. A drug molecule will display the highest potency when its bioactive conformation matches very well with the binding pocket. Generally speaking, some residues in the binding pocket of a receptor protein might be conformationally flexible, while the others are rigid. Therefore, optimizing the interactions with the conformationally flexible residues in the binding pocket should be an effective way to improve the potency of a drug.

Cytochrome *bc*<sub>1</sub> complex (EC 1.10.2.2, *bc*<sub>1</sub>) is well known as an essential component of the cellular respiratory chain and the photosynthetic apparatus in photosynthetic bacteria. It is

known to catalyze the electron transfer from quinol to a soluble cytochrome *c* (cyt *c*) and couple this electron transfer to the translocation of protons across the membrane.<sup>2–5</sup> The *bc*<sub>1</sub> complex has been found in the plasma membrane of bacteria and in the inner mitochondrial membrane of eukaryotes. Due to its crucial role in the life cycle, the *bc*<sub>1</sub> complex has been identified as a promising target for new drugs and agricultural fungicides.<sup>6,7</sup> For example, malaria, especially chloroquine- and multidrug-resistant *Plasmodium falciparum* malaria, remains a major threat to over 40% of the world's population and is

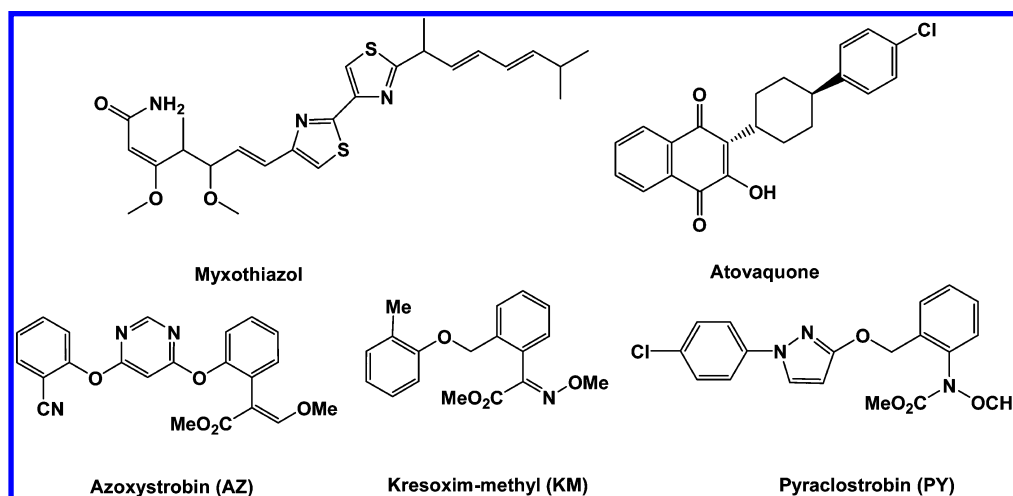
- (2) Kim, H.; Xia, D.; Yu, C. A.; Xia, J. Z.; Kachurin, A. M.; Zhang, L.; Yu, L.; Deisenhofer, J. *Proc. Natl. Acad. Sci. U.S.A.* **1998**, *95*, 8026–8033.
- (3) Gao, X. G.; Wen, X. L.; Yu, G. A.; Esser, L.; Tsao, S.; Quinn, B.; Zhang, L.; Yu, L. D.; Xia, D. *Biochemistry* **2002**, *41*, 11692–11702.
- (4) Berry, E. A.; Huang, L. S. *FEBS Lett.* **2003**, *555*, 13–20.
- (5) Esser, L.; Quinn, B.; Li, Y. F.; Zhang, M. Q.; Elberry, M.; Yu, L. D.; Yu, C. A.; Xia, D. *J. Mol. Biol.* **2004**, *341*, 281–302.
- (6) Sauter, H.; Steglich, W.; Anke, T. *Angew. Chem., Int. Ed.* **1999**, *38*, 1328–1349.
- (7) Xiang, H.; McSurdy-Freed, J.; Moorthy, G. S.; Hugger, E.; Bambal, R.; Han, C.; Ferrer, S.; Gargallo, D.; Davis, C. B. *J. Pharm. Sci.* **2006**, *95*, 2657–2672.

<sup>†</sup> Central China Normal University.

<sup>‡</sup> Tsinghua University.

<sup>§</sup> University of Kentucky.

(1) Ladbury, J. E. *Thermochim. Acta* **2001**, *380*, 209–215.

Scheme 1. Chemical Structures of Some Representative  $bc_1$  Inhibitors

associated with about a hundred million clinical cases every year. Atovaquone (Scheme 1) has been used in treating multidrug-resistant malaria and for prophylaxis in areas with chloroquine resistance for many years.<sup>8–12</sup> The action mechanism of Atovaquone is to inhibit the  $bc_1$  complex by binding to the ubiquinol oxidation pocket of the  $bc_1$  complex, where it interacts with the Rieske iron–sulfur protein.<sup>11,12</sup> In addition, a number of  $Q_0$ -specific inhibitors of the  $bc_1$  complex, always named  $Q_0$ I fungicides, have been introduced into the agricultural fungicide market.<sup>13,14</sup> The first  $Q_0$ I fungicides entered the market in 1996, including azoxystrobin (AZ) and kresoxim-methyl (KM) (Scheme 1), two synthetic analogues of the natural antifungal compound strobilurin A. With a distributor sale value of over US\$900 million apiece in 2008, AZ currently represents one of the most important fungicides in the world.

According to structural information determined by crystallographic studies, Xia et al.<sup>5</sup> suggested that the existing  $bc_1$  inhibitors could be grouped into three classes: class P, class N, and class PN. Class P inhibitors, binding at the  $Q_0$  site, include famoxadone, stigmatellin, 5-undecyl-6-hydroxy-4,7-dioxobenzothiazole (UHDBT), methoxyacrylate stilbene (MOAS), myxothiazol, AZ, KM, pyraclostrobin (PY), and many others. Class N inhibitors, targeting the  $Q_i$  site, include antimycin A and diuron. Class PN inhibitors, with the capability of binding to both the  $Q_0$  and  $Q_i$  sites, include 2-*n*-nonyl-4-hydroxyquinoline *N*-oxide (NQNO) and possibly funiculosin. Among these inhibitors, MOA-type inhibitors, such as strobilurin, oudemansin, and AZ, are very important due to their great commercial success and potential role in elucidating the molecular mechanism of  $bc_1$  function. However, these commercial inhibitors as agricultural fungicides or drugs are suffering from the rapid development of resistance associated with site mutations of the

$bc_1$  complex. Therefore, discovery of new  $bc_1$  inhibitors with a higher potency is of great interest.<sup>15–17</sup>

X-ray diffraction structures of the free  $bc_1$  complex and its complexes with various MOA-type inhibitors revealed that the conformation of the MOA moiety in the binding pocket is well conserved,<sup>3,5</sup> especially for the methoxy and carbonyl oxygen atoms, which makes it possible to identify common structural features that are important for binding. In addition, the  $Q_0$  pocket is hydrophobic and exceptionally rich in highly conserved residues (Supporting Information, Figure 1s). Most importantly, the Ar–Ar stacking interactions with the hydrophobic pocket formed by the side chains of Phe274, Phe128, Ile146, Pro270, Ala277, Leu294, Met124, and Ile298 (numbered according to the cyt *b* subunit of the bovine  $bc_1$ ) have an important contribution to the binding affinity of inhibitors.<sup>3,5</sup> It is noteworthy that the side chains of all these hydrophobic residues showed conformational stability during the simulation, except for the phenyl group of Phe274, which exhibited significant conformational flexibility in different complexes. The conformational flexibility of the Phe274 side chain allows us to optimize the corresponding Ar–Ar interactions. However, due to the existence of the linear cyano group in AZ, the phenyl ring of the cyanophenoxyl group is almost vertical to the pyrimidyl ring. As a result, the pyrimidyl ring does not parallel well with the phenyl ring of Phe274 to reach an ideal Ar–Ar interaction. In contrast, myxothiazol has a higher potency than AZ because its thiazole ring parallels well with the phenyl group of Phe274. These facts suggest that improving the Ar–Ar interactions between the side-chain of inhibitors and the phenyl of Phe274 may be an effective way to design and discover new, more potent inhibitors of  $bc_1$  complex.

On the basis of the above premises, the development of new, more potent  $bc_1$  inhibitors by improving the Ar–Ar interactions of AZ is the main strategy of this work. Without altering the main structural features of MOA-type inhibitors, we first designed the molecular framework I (Scheme 2). As an important kind of five-membered aromatic scaffold with broad-spectrum biological activities, the pyrazole ring appears in many

(8) Yeates, C. L.; et al. *J. Med. Chem.* **2008**, *51*, 2845–2852.

(9) Fry, M.; Pudney, M. *Biochem. Pharmacol.* **1992**, *43*, 1545–1553.

(10) Kessl, J. J.; Meshnick, S. R.; Trumpower, B. L. *Trends Parasitol.* **2007**, *23*, 494–501.

(11) Mather, M. W.; Darrouzet, E.; Valkova-Valchanova, M.; Cooley, J. W.; McIntosh, M. T.; Daldal, F.; Vaidya, A. B. *J. Biol. Chem.* **2005**, *280*, 27458–27465.

(12) Kessl, J. J.; Lange, B. B.; Merbitz-Zahradnik, T.; Zwicker, K.; Hill, P.; Meunier, B.; Palsdottir, H.; Hunte, C.; Meshnick, S.; Trumpower, B. L. *J. Biol. Chem.* **2003**, *278*, 31312–31318.

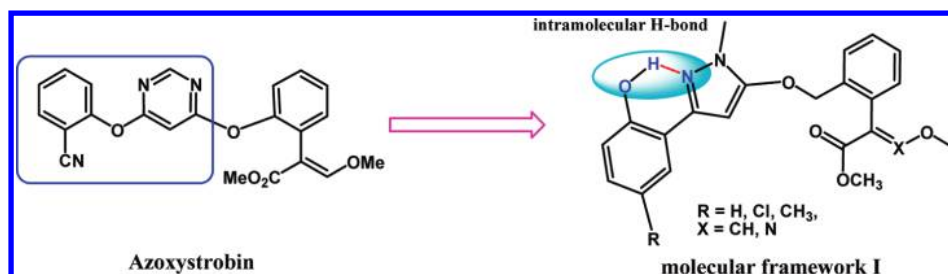
(13) Bartlett, D. W.; Clough, J. M.; Godwin, J. R.; Hall, A. A.; Hamer, M.; Parr-Dobrzanski, B. *Pest Manag. Sci.* **2002**, *58*, 649–662.

(14) Balba, H. J. *Environ. Sci. Health B* **2007**, *42*, 441–451.

(15) Bolgunas, S.; Clark, D. A.; Hanna, W. S.; Mauvais, P. A.; Pember, S. O. *J. Med. Chem.* **2006**, *49*, 4762–4766.

(16) Ding, M. G.; di Rago, J. P.; Trumpower, B. L. *J. Biol. Chem.* **2006**, *281*, 36036–36043.

(17) Kolesova, G. M.; Belyakova, M. M.; Mamedov, M. D.; Yaguzhinsky, L. S. *Biochemistry-Moscow* **2000**, *65*, 578–582.

**Scheme 2.** Proposed Structures of New *bc*<sub>1</sub> Inhibitors with an Intramolecular Hydrogen Bond

commercial drugs.<sup>18–20</sup> Hence, we replaced the pyrimidine ring of AZ with a methylpyrazole ring, as shown in Scheme 2. Meanwhile, an *ortho*-hydroxy group was designed to replace the cyano group, with the expectation that an intramolecular hydrogen bond between the hydroxy group and the N(1) atom of pyrazole ring could be formed, making it possible for the pyrazole ring to be perfectly parallel with the phenyl group of Phe274, improving the Ar–Ar interactions. In addition, in order to adjust the hydrophobic property of the designed compounds, some functional groups, such as Cl and CH<sub>3</sub>, were also introduced into the R-position of the phenyl moiety.

The strategy we proposed for the selection of compounds to be synthesized makes use of computational simulation protocols. These allow us to analyze the key interactions at the atomic level between the selected compounds and the *bc*<sub>1</sub> complex. As a result, one compound with a *K*<sub>i</sub> value of 570 pM against porcine *bc*<sub>1</sub> complex was discovered. To our knowledge, it is so far the first *bc*<sub>1</sub> inhibitor discovered through structure-based design with subnanomolar *K*<sub>i</sub> potency. The synthesis, *in vitro* enzymatic assay, and subsequent enzymatic kinetic study of this *bc*<sub>1</sub> inhibitor are reported in this work. Its excellent potency and interesting characteristics of enzymatic kinetic behavior indicate that this compound could be used as a specific probe for further elucidating the mechanism of *bc*<sub>1</sub> function and as a new lead compound for future drug discovery.

## Materials and Methods

### 1. Computational Methods. Homology Modeling of the Porcine Cytochrome *b* Subunit (cyt *b*).

In order to study the binding of a set of representative inhibitors with the porcine mitochondrial cytochrome *bc*<sub>1</sub> complex, a homology model of the cyt *b* was built by using the complete crystal structure of bovine heart cytochrome *bc*<sub>1</sub> in complex with AZ (PDB entry 1SQB) as the template and the Homology module of the InsightII program (version 2000, Accelrys, Inc., San Diego, CA). As one of the available cytochrome *bc*<sub>1</sub> crystal structures containing inhibitors, the AZ-bound *bc*<sub>1</sub> complex was selected as the template because of its structural similarity to the compounds used in this study. The sequence alignment between the porcine cyt *b* and the same subunit of the template was generated by ClusterW with the Blosum scoring function. The best alignment was selected according to both the alignment score and the reciprocal positions of the conserved residues, especially those in or close to the inhibitor-binding sites of the template. The coordinates of the conserved regions, including the two heme groups at the *b*<sub>L</sub> and *b*<sub>H</sub> sites, were transformed directly from the template structure, whereas the nonequivalent residues were mutated from the template to the corresponding ones in the porcine cyt *b*. The side chains of these nonconserved residues were relaxed by using the Homology module of InsightII, in order

to remove any possible steric overlap (or hindrance) with the neighboring conserved residues. The structures of other subunits of the porcine cyt *bc*<sub>1</sub> complex were not modeled due to the shortage of their amino acid sequences of some of the subunits. In order to view the structural integrity, the structures of other subunits of the porcine cyt *bc*<sub>1</sub> complex were directly copied from the template, proving their high homology to the bovine heart cyt *bc*<sub>1</sub> complex.

After initial coordinates were generated, all the ionizable residues of cyt *b* were set to the standard protonation states. A careful check of the structural model allowed the proton to be assigned to the N<sub>D1</sub> atoms for all the His residues under the physiological condition (pH ~7.4), including His83, His97, His182, and His196 coordinated with the central irons of the two heme groups. As the His residues are coordinated optimally with the two heme groups, as seen from the crystal structure, these residues and heme groups were always fixed in the following energy minimization steps. The initial 3D model of the porcine cyt *b* was energy-minimized by using the Sander module of the Amber8 program<sup>21</sup> suite with a nonbonded cutoff of 12 Å and a conjugate gradient minimization method. The heme groups were treated at its oxidized state, and the input parameters of these heme groups were directly adopted from Izrailev et al.<sup>22</sup> in their steered molecular dynamics simulations. The energy minimization was performed in the gas phase, first for 5000 steps with the backbone atoms fixed while the side-chain atoms were relaxed, and then for another 1000 steps with the side-chain atoms constrained in order to relax the backbone. After two rounds of these partial energy-minimization runs, the convergence criterion of 0.001 kcal mol<sup>-1</sup> Å<sup>-1</sup> was quickly achieved in a full energy minimization.

### Molecular Docking.

As observed from the crystal structure, AZ is bound in the Q<sub>o</sub> site, which is formed by loop *ef*, helices cd1 and cd2, and part of the helices B, C, E, and F. Considering the structural similarity of AZ with other inhibitors, this Q<sub>o</sub> site was also selected as a binding site for other inhibitors. Based on the 3D model of the porcine cyt *b*, the AutoDock 4.0 program<sup>23</sup> was applied to dock these inhibitors into the Q<sub>o</sub> binding site. The Gasteiger charges were used for these inhibitors. To select the best set of docking parameters and to test the reliability of the docking results, the AZ was first docked into the Q<sub>o</sub> binding site. In the docking process, a conformational search was performed for the AZ molecule using the Solis and Wets local search method, and the Lamarkian genetic algorithm (LGA) was applied for the conformational search of the binding complex of AZ with porcine cyt *b*. Among a series of docking parameters, the grid size was set to be 40 × 40 × 40, and the used grid space was the default value of 0.375 Å. The interaction energy that resulted from probing the porcine cyt *b* with the AZ molecule was assessed by the standard AutoDock scoring function. Among a set of 50 candidates of the docked complex structures, the best one was first selected according

(18) McDonald, E.; Jones, K.; Brough, P. A.; Drysdale, M. J.; Workman, P. *Curr. Top. Med. Chem.* **2006**, *6*, 1193–1203.  
 (19) Lamberth, C. *Heterocycles* **2007**, *71*, 1467–1502.  
 (20) Hansen, J.; et al. *Bioorg. Med. Chem. Lett.* **2008**, *18*, 4692–4695.

(21) Pearlman, D. A.; Case, D. A.; Caldwell, J. W.; Ross, W. S.; Cheatham, T. E.; Debolt, S.; Ferguson, D.; Seibel, G.; Kollman, P. *Comput. Phys. Commun.* **1995**, *91*, 1–41.  
 (22) Izrailev, S.; Crofts, A. R.; Berry, E. A.; Schulten, K. *Biophys. J.* **1999**, *77*, 1753–1768.  
 (23) Morris, G. M.; Goodsell, D. S.; Halliday, R. S.; Huey, R.; Hart, W. E.; Belew, R. K.; Olson, A. J. *J. Comput. Chem.* **1998**, *19*, 1639–1662.

to the interaction energy and was then compared with the conformation of AZ extracted from the crystal structure. By tuning the docking parameters, the final AZ-cyt *b* complex was obtained, based on the smallest root-mean-square deviation (rmsd) of the docked conformation of AZ from its conformation in the crystal structure. The same set of docking parameters were adopted in the molecular docking of other inhibitors, including KM, PY, **5a–d**, and **6a–d**, into the Q<sub>o</sub> binding site of cyt *b*.

All the complex structures derived from molecular docking were used as starting structures for further energy minimizations using the Sander module of the Amber8 program before the final binding structures were achieved. The atomic charges used for these inhibitors were the restrained electrostatic potential (RESP) charges, determined by using the standard RESP procedure implemented in the Antechamber module of the Amber8 program following the electronic structure and electrostatic potential calculations at the HF/6-31G\* level. The energy minimization process was similar to that used for modeling the porcine cyt *b*, i.e., first fixing the backbone atoms of the protein, in order to relax the side chains and the docked inhibitor molecule. Energy minimization was then performed on the whole complex until the convergence criterion of 0.001 kcal mol<sup>-1</sup> Å<sup>-1</sup> was reached.

**Binding Energy Calculations.** Due to the fact that only the structure of cyt *b* of the porcine bc<sub>1</sub> complex was modeled, and due to the expected geometric symmetry of the dimer structure of the porcine bc<sub>1</sub> complex, the binding free energy for each inhibitor with the porcine bc<sub>1</sub> complex was represented by the binding free energy for each inhibitor with the cyt *b*. Such an approximation should be reasonable, as all the other subunits are far away from the Q<sub>o</sub> binding site and have no direct interactions with the inhibitors binding at the Q<sub>o</sub> site. Their effects on the inhibitor binding are on the long-range interactions; therefore, such long-range interactions can be treated as background, without significant influence on the calculated binding free energy ( $\Delta G_{\text{bind}}$ ). On the basis of the modeled complex structure of porcine cyt *b* bound with inhibitors, the binding free energy for each of the minimized complexes was estimated by using the molecular mechanics Poisson–Boltzmann surface area (MM-PBSA) method.<sup>24</sup>

In the MM-PBSA calculations, the free energy of inhibitor binding,  $\Delta G_{\text{bind}}$ , was calculated from the difference between the free energies of the complex ( $G_{\text{complex}}$ ) and the free cyt *b* ( $G_{\text{cytb}}$ ) and free inhibitor ( $G_{\text{inhibitor}}$ ) as

$$\Delta G_{\text{bind}} = G_{\text{complex}} - (G_{\text{cytb}} + G_{\text{inhibitor}}) \quad (1)$$

$\Delta G_{\text{bind}}$  was evaluated as a sum of the changes in the MM gas-phase binding energy ( $\Delta E_{\text{bind}}$ ), solvation free energy ( $\Delta G_{\text{solv}}$ ), and entropy contribution ( $-T\Delta S$ ):

$$\Delta G_{\text{bind}} = \Delta E_{\text{bind}} - T\Delta S \quad (2)$$

$$\Delta E_{\text{bind}} = \Delta E_{\text{MM}} + \Delta G_{\text{solv}} \quad (3)$$

$$\Delta G_{\text{solv}} = \Delta G_{\text{PB}} + \Delta G_{\text{np}} \quad (4)$$

$$\Delta G_{\text{np}} = \gamma \text{SASA} \quad (5)$$

The electrostatic solvation free energy was calculated by the finite-difference solution to the Poisson–Boltzmann (PB) equation ( $\Delta G_{\text{PB}}$ ) as implemented in the Delphi program.<sup>25,26</sup> The dielectric constants used were 1 for the solute and 78.5 for the solvent. The SASA was calculated by the default surface area calculation program in the MM-PBSA module of the Amber8 program with the default  $\gamma = 0.0072$  kcal Å<sup>-2</sup>. The entropy contribution,  $-T\Delta S$ , to the binding

free energy was calculated at  $T = 300$  K by using an in-house program that has proven to be reliable in our other studies.<sup>27–33</sup>

**2. Syntheses of the Title Compounds.** Unless noted otherwise, reagents and starting materials **1a–c** were purchased from commercial suppliers and used without further purification whereas all solvents were redistilled before use. <sup>1</sup>H NMR spectra were recorded on a Mercury-Plus 400 spectrometer in CDCl<sub>3</sub> with TMS as the internal reference. MS spectra were determined using a Trace MS 2000 organic mass spectrometry. Elementary analyses were performed on a Vario EL III elemental analysis instrument. Melting points were taken on a Büchi B-545 melting point apparatus and are uncorrected. Intermediates **2a–c**, **3a–c**, and **4a,b** were prepared according to the reported methods.<sup>34–36</sup>

**Preparation of 4-Hydroxycoumarins 2a–c.** In a 250 mL two-neck round-bottom flask, 36 mmol of *o*-hydroxyacetophenone **1** was added to 6.3 g of NaH (180 mmol, 70%, dispersion in mineral oil) in anhydrous toluene (100 mL). After the evolution of hydrogen had ceased, 6 mL of diethyl carbonate in anhydrous toluene (20 mL) was added dropwise during 30 min, and the mixture was refluxed with stirring for 3 h. After the mixture cooled to room temperature, the precipitate was filtered off and washed with 20 mL of toluene. The combined toluene solutions were concentrated on a rotary evaporator, and the residue was poured into 100 mL of water and acidified with 2 N hydrochloric acid. The resulting precipitate was filtered off and recrystallized from ethanol to give a white solid. Yields for **2a**, **2b**, and **2c** are 85%, 72%, and 75%, respectively.

**Preparation of 3-(2-Hydroxy-5-substituted phenyl)-1-methyl-1H-pyrazol-5(4H)-ones 3a–c.** In a 100 mL three-neck round-bottom flask, 6 mmol of 6-substituted 4-hydroxycoumarins **2**, 5.6 g (12 mmol) of methylhydrazine, and 40 mL of ethanol were added gradually. The reaction was refluxed under N<sub>2</sub> flow until the material was completely transformed by TLC. The resulting mixture was concentrated on a rotary evaporator to give the crude products. The white crystal **3** could be obtained by recrystallization of the crude products from ethanol. Yields for **3a**, **3b**, and **3c** are 81%, 92%, and 90%, respectively.

**General Procedure for the Synthesis of Target Compounds 5a–d.** A mixture of 5.0 mmol of 3-(2-hydroxy-5-substituted phenyl)-1-methyl-1H-pyrazol-5(4H)-one **3** and 0.82 g (6.0 mmol) of anhydrous K<sub>2</sub>CO<sub>3</sub> in dry acetone (20 mL) was stirred and refluxed for 0.5 h, followed by the addition of 5.0 mmol of intermediate **4**. The reaction was continued for 5–8 h under reflux. The resulting mixture was cooled to room temperature and filtered off by suction, and the solvent was evaporated to give the crude product, followed by chromatography purification on silica using a mixture of petroleum ether and acetone (12:1) as eluent to give the target compounds **5a–d** in yields of 67–84%.

**Data for 5a:** yield, 74%; mp 129–131 °C; <sup>1</sup>H NMR (400 MHz, CDCl<sub>3</sub>)  $\delta$  3.69 (s, 3H, NCH<sub>3</sub>), 3.73 (s, 3H, COOCH<sub>3</sub>), 3.85 (s, 3H,

- (24) Kollman, P.; Massova, I.; Reyes, C.; Kuhn, B.; Huo, S.; Chong, L.; Lee, M.; Duan, Y.; Wang, W.; Donini, O.; Cieplak, P.; Srivivasan, J.; Case, D.; Cheatham, T. E. *Acc. Chem. Res.* **2000**, *33*, 889–897.  
 (25) Jayaram, B.; Sharp, K. A.; Honig, B. *Biopolymers* **1989**, *28*, 975–993.  
 (26) Sanner, M. F.; Olson, A. J.; Spehner, J. C. *Biopolymers* **1996**, *38*, 305–320.

- (27) Ji, F. Q.; Niu, C. W.; Chen, C. N.; Chen, Q.; Yang, G. F.; Xi, Z.; Zhan, C. G. *ChemMedChem* **2008**, *3*, 1203–1206.  
 (28) Pan, Y. M.; Gao, D. Q.; Yang, W. C.; Cho, H.; Yang, G. F.; Tai, H. H.; Zhan, C. G. *Proc. Natl. Acad. Sci. U.S.A.* **2005**, *102*, 16656–16661.  
 (29) Gao, D. Q.; Cho, H.; Yang, W. C.; Pan, Y. M.; Yang, G. F.; Tai, H. H.; Zhan, C. G. *Angew. Chem., Int. Ed.* **2006**, *45*, 653–657.  
 (30) Pan, Y. M.; Gao, D. Q.; Yang, W. C.; Cho, H.; Zhan, C. G. *J. Am. Chem. Soc.* **2007**, *129*, 13537–13543.  
 (31) Zhan, C. G.; Zheng, F.; Landry, D. W. *J. Am. Chem. Soc.* **2003**, *125*, 2462–2474.  
 (32) Xiong, Y.; Li, Y.; He, H. W.; Zhan, C. G. *Bioorg. Med. Chem. Lett.* **2007**, *17*, 5186–5190.  
 (33) Pan, Y. M.; Gao, D. Q.; Zhan, C. G. *J. Am. Chem. Soc.* **2008**, *130*, 5140–5149.  
 (34) Desai, N. J.; Suresh, S. *J. Org. Chem.* **1957**, *22*, 388–390.  
 (35) Froggett, J. A.; Hockley, M. H.; Titman, R. B. *J. Chem. Res. (S)* **1997**, 30–31.  
 (36) Kim, B. T.; Park, N. K.; Choi, G. J.; Kim, J. C.; Pak, C. S. Patent WO 0112585, 2001; *Chem. Abstr.* **2001**134193207.

=CH–OCH<sub>3</sub>), 5.07 (s, 2H, CH<sub>2</sub>), 5.82 (s, 1H, HetH), 6.87 (t, *J* = 8.0 Hz, 1H, ArH), 6.99 (d, *J* = 8.0 Hz, 1H, ArH), 7.15–7.23 (m, 3H, ArH), 7.38–7.43 (m, 2H, ArH), 7.53 (dd, *J* = 3.6 Hz, *J* = 4.8 Hz, 1H, ArH), 7.63 (s, 1H, =CH–OCH<sub>3</sub>); EI-MS *m/z* (relative intensity) 395 ([M + 1]<sup>+</sup>, 17), 394 (M<sup>+</sup>, 100), 362 (19), 330 (14), 205 (60), 204 (42), 188 (13), 145 (83), 131 (23), 117 (38), 115 (25), 102 (51). Anal. Calcd for C<sub>22</sub>H<sub>22</sub>N<sub>2</sub>O<sub>5</sub>: C, 66.99; H, 5.62; N, 7.10. Found: C, 67.19; H, 5.38; N, 7.21.

**Data for 5b:** yield, 84%; mp 143–145 °C; <sup>1</sup>H NMR (400 MHz, CDCl<sub>3</sub>) δ 2.29 (s, 3H, Ar–CH<sub>3</sub>), 3.68 (s, 3H, NCH<sub>3</sub>), 3.70 (s, 3H, COOCH<sub>3</sub>), 3.84 (s, 3H, =CH–OCH<sub>3</sub>), 5.06 (s, 2H, CH<sub>2</sub>), 5.81 (s, 1H, HetH), 6.88 (d, *J* = 8.0 Hz, 1H, ArH), 6.98 (d, *J* = 8.4 Hz, 1H, ArH), 7.20–7.24 (m, 2H, ArH), 7.37–7.41 (m, 2H, ArH), 7.52 (dd, *J* = 3.2 Hz, *J* = 4.8 Hz, 1H, ArH), 7.62 (s, 1H, =CH–OCH<sub>3</sub>); EI-MS *m/z* (relative intensity) 409 ([M + 1]<sup>+</sup>, 6), 408 (M<sup>+</sup>, 44), 205 (23), 204 (24), 175 (10), 146 (11), 145 (100), 131 (28), 103 (34). Anal. Calcd for C<sub>23</sub>H<sub>24</sub>N<sub>2</sub>O<sub>5</sub>: C, 67.63; H, 5.92; N, 6.86. Found: C, 67.36; H, 5.83; N, 6.90.

**Data for 5c:** yield, 81%; mp 189–191 °C; <sup>1</sup>H NMR (600 MHz, CDCl<sub>3</sub>) δ 3.68 (s, 3H, NCH<sub>3</sub>), 3.73 (s, 3H, COOCH<sub>3</sub>), 3.88 (s, 3H, =CH–OCH<sub>3</sub>), 5.06 (s, 2H, CH<sub>2</sub>), 5.73 (s, 1H, HetH), 6.88 (d, *J* = 8.8 Hz, 1H, ArH), 7.08 (dd, *J* = 1.4 Hz, *J* = 9.0 Hz, 1H, ArH), 7.21 (dd, *J* = 3.6 Hz, *J* = 5.2 Hz, 1H, ArH), 7.33 (d, *J* = 2.4 Hz, 1H, ArH), 7.37 (dd, *J* = 3.2 Hz, *J* = 5.6 Hz, 2H, ArH), 7.50 (dd, *J* = 3.6 Hz, *J* = 5.2 Hz, 1H, ArH), 7.64 (s, 1H, =CH–OCH<sub>3</sub>); EI-MS *m/z* (relative intensity) 428 (M<sup>+</sup>, 2), 204 (36), 189 (14), 160 (32), 144 (100), 128 (29), 115 (26), 101 (29), 91 (34). Anal. Calcd for C<sub>22</sub>H<sub>21</sub>ClN<sub>2</sub>O<sub>5</sub>: C, 61.61; H, 4.94; N, 6.53. Found: C, 61.35; H, 5.15; N, 6.59.

**Data for 5d:** yield, 67%; mp 150–152 °C; <sup>1</sup>H NMR (600 MHz, CDCl<sub>3</sub>) δ 3.66 (s, 3H, NCH<sub>3</sub>), 3.86 (s, 3H, COOCH<sub>3</sub>), 4.08 (s, 3H, =N–OCH<sub>3</sub>), 5.07 (s, 2H, CH<sub>2</sub>), 5.82 (s, 1H, HetH), 6.86 (t, *J* = 4.4 Hz, 1H, ArH), 6.98 (d, *J* = 7.8 Hz, 1H, ArH), 7.15–7.25 (m, 2H, ArH), 7.40–7.54 (m, 4H, ArH); EI-MS *m/z* (relative intensity) 395 (M<sup>+</sup>, 42), 206 (10), 205 (20), 189 (28), 160 (41), 146 (31), 131 (96), 118 (37), 116 (100), 115 (19), 89 (27). Anal. Calcd for C<sub>21</sub>H<sub>21</sub>N<sub>3</sub>O<sub>5</sub>: C, 63.79; H, 5.35; N, 10.63. Found: C, 63.52; H, 5.58; N, 10.44.

### General Procedure for the Synthesis of Target Compounds

**6.** A reaction system with 1.0 mmol of compounds **5a,b** and 0.16 g (1.2 mmol) of anhydrous K<sub>2</sub>CO<sub>3</sub> or 0.12 g (1.2 mmol) of triethylamine in dry *N,N*-dimethylformamide (DMF) (6 mL) was stirred at room temperature for 0.5 h, followed by the addition of 1.1 mmol of halogenated compounds or substituted benzoyl chloride. The reaction was continued for 2–24 h. The resulting mixture was poured into 20 mL of water, extracted with ethyl acetate (10 mL × 3), washed with saturated sodium chloride (10 mL × 3), dried with anhydrous magnesium sulfate, and filtered off with suction. The solvent was evaporated to give the crude, which was purified by chromatography on silica using a mixture of petroleum ether and acetone (20:1) as eluent to give the target compounds **6a–d** in yields of 46–82%.

**Data for 6a:** yield, 78%; mp 117–119 °C; <sup>1</sup>H NMR (400 MHz, CDCl<sub>3</sub>) δ 3.68 (s, 3H, NCH<sub>3</sub>), 3.70 (s, 3H, COOCH<sub>3</sub>), 3.73 (s, 3H, =CH–OCH<sub>3</sub>), 3.86 (s, 3H, Ar–OCH<sub>3</sub>), 5.06 (s, 2H, CH<sub>2</sub>), 5.81 (s, 1H, HetH), 6.85 (t, *J* = 8.0 Hz, 1H, ArH), 6.98 (d, *J* = 7.2 Hz, 1H, ArH), 7.07 (dd, *J* = 3.6 Hz, *J* = 5.6 Hz, 1H, ArH), 7.16–7.24 (m, 2H, ArH), 7.38–7.42 (m, 2H, ArH), 7.54 (dd, *J* = 3.6 Hz, *J* = 5.6 Hz, 1H, ArH), 7.64 (s, 1H, =CH–OCH<sub>3</sub>); EI-MS *m/z* (relative intensity) 410 ([M + 1]<sup>+</sup>, 3), 408 (M<sup>+</sup>, 2), 394 (100), 378 (10), 376 (31), 375 (83), 361 (17), 318 (13), 161 (16), 145 (26), 118 (21), 115 (14), 102 (29). Anal. Calcd for C<sub>23</sub>H<sub>24</sub>N<sub>2</sub>O<sub>5</sub>: C, 67.63; H, 5.92; N, 6.86. Found: C, 67.83; H, 6.01; N, 6.76.

**Data for 6b:** yield, 46%; mp 152–153 °C; <sup>1</sup>H NMR (400 MHz, CDCl<sub>3</sub>) δ 2.32 (s, 3H, Ar–CH<sub>3</sub>), 3.70 (s, 3H, NCH<sub>3</sub>), 3.77 (s, 3H, COOCH<sub>3</sub>), 3.84 (s, 3H, =CH–OCH<sub>3</sub>), 3.87 (s, 3H, Ar–OCH<sub>3</sub>), 5.06 (s, 2H, CH<sub>2</sub>), 6.08 (s, 1H, HetH), 6.85 (d, *J* = 8.4 Hz, 1H, ArH), 7.09 (t, *J* = 7.2 Hz, 1H, ArH), 7.21 (d, *J* = 7.8 Hz, 1H, ArH), 7.36–7.40 (m, 2H, ArH), 7.53 (t, *J* = 7.2 Hz, 1H, ArH),

7.60 (s, 1H, =CH–OCH<sub>3</sub>), 7.71 (s, 1H, ArH); EI-MS *m/z* (relative intensity) 423 ([M + 1]<sup>+</sup>, 8), 422 (M<sup>+</sup>, 9), 217 (13), 206 (18), 205 (91), 173 (14), 146 (13), 145 (100), 131 (19), 130 (20), 116 (24), 103 (12). Anal. Calcd for C<sub>24</sub>H<sub>26</sub>N<sub>2</sub>O<sub>5</sub>: C, 68.23; H, 6.20; N, 6.63. Found: C, 68.43; H, 5.99; N, 6.65.

**Data for 6c:** yield, 82%; mp 83–85 °C; <sup>1</sup>H NMR (400 MHz, CDCl<sub>3</sub>) δ 3.65 (s, 3H, NCH<sub>3</sub>), 3.67 (s, 3H, COOCH<sub>3</sub>), 3.70 (s, 3H, =CH–OCH<sub>3</sub>), 4.91 (s, 2H, Ph–OCH<sub>2</sub>), 5.15 (s, 2H, Het–OCH<sub>2</sub>), 6.13 (s, 1H, HetH), 6.99–7.04 (m, 2H, ArH), 7.18 (dd, *J* = 4.0 Hz, *J* = 5.2 Hz, 1H, ArH), 7.31–7.39 (m, 6H, ArH), 7.43–7.48 (m, 3H, ArH), 7.51 (s, 1H, =CH–OCH<sub>3</sub>), 7.94 (d, *J* = 7.6 Hz, 1H, ArH); EI-MS *m/z* (relative intensity) 484 (M<sup>+</sup>, 9), 280 (13), 204 (100), 177 (21), 174 (14), 173 (23), 144 (98), 131 (22), 117 (16), 114 (54), 103 (37), 101 (35). Anal. Calcd for C<sub>29</sub>H<sub>28</sub>N<sub>2</sub>O<sub>5</sub>: C, 71.88; H, 5.82; N, 5.78. Found: C, 71.72; H, 5.62; N, 5.62.

**Data for 6d:** yield, 81%; mp 76–77 °C; <sup>1</sup>H NMR (400 MHz, CDCl<sub>3</sub>) δ 3.61 (s, 3H, NCH<sub>3</sub>), 3.75 (s, 3H, COOCH<sub>3</sub>), 3.87 (s, 3H, =CH–OCH<sub>3</sub>), 5.39 (s, 2H, CH<sub>2</sub>), 5.76 (s, 1H, HetH), 7.11–7.19 (m, 2H, ArH), 7.28–7.33 (m, 3H, ArH), 7.34–7.40 (m, 3H, ArH), 7.61 (d, *J* = 7.2 Hz, 1H, ArH), 7.69 (s, 1H, =CH–OCH<sub>3</sub>), 7.87 (d, *J* = 7.8 Hz, 1H, ArH), 7.99 (d, *J* = 7.8 Hz, 1H, ArH), 8.23 (t, *J* = 7.2 Hz, 1H, ArH); EI-MS *m/z* (relative intensity) 517 ([M + 1]<sup>+</sup>, 6), 516 (M<sup>+</sup>, 8), 484 (20), 456 (24), 147 (14), 145 (43), 144 (23), 131 (17), 123 (100), 115 (22), 103 (23), 102 (14). Anal. Calcd for C<sub>29</sub>H<sub>25</sub>FN<sub>2</sub>O<sub>6</sub>: C, 67.43; H, 4.88; N, 5.42. Found: C, 67.15; H, 4.69; N, 5.12.

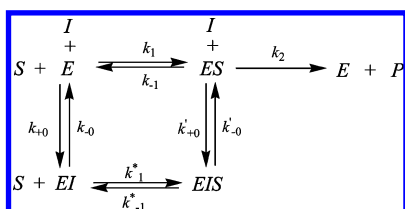
**X-ray Diffraction.** A colorless block of **5b** (0.20 mm × 0.20 mm × 0.10 mm) was mounted on a quartz fiber. Cell dimensions and intensities were measured at 299 K on a Bruker SMART CCD area detector diffractometer with graphite-monochromated Mo K $\alpha$  radiation ( $\lambda = 0.71073$  Å);  $\theta_{\max} = 22.13$ ; 6204 measured reflections; 3658 independent reflections ( $R_{\text{int}} = 0.0229$ ), of which 2701 had  $|F_o| > 2|F_c|$ . Data were corrected for Lorentz and polarization effects and for absorption ( $T_{\min} = 0.9819$ ;  $T_{\max} = 0.9909$ ). The structure was solved by direct methods using SHELXS-97;<sup>37</sup> all other calculations were performed with Bruker SAINT System and Bruker SMART programs.<sup>38</sup> Full-matrix least-squares refinement based on  $F^2$  using the weight of  $1/[\sigma^2(F_o)^2 + (0.0934P)^2 + 0.1767P]$  gave final values of  $R = 0.0570$ ,  $\omega R = 0.1576$ , and  $\text{GOF}(F) = 1.055$  for 289 variables and 1634 contributing reflections. Maximum shift/error = 0.000(3), max/min residual electron density = 0.209/–0.169 e Å<sup>–3</sup>. Hydrogen atoms were observed and refined with a fixed value of their isotropic displacement parameter.

**3. Inhibitory Kinetics of Porcine *bc*<sub>1</sub> Complex.** The preparation of succinate–cytochrome *c* reductase (SCR, mixture of respiratory complex II and *bc*<sub>1</sub> complex) from porcine heart was essentially as reported.<sup>39</sup> The activity of SCR in catalyzing the oxidation of succinate by cytochrome *c* was determined in 1.8 mL of reaction mixture containing 100 mM PBS (pH 7.4), 0.3 mM EDTA, 20 mM succinate, 60 μM oxidized cytochrome *c*, and an appropriate amount of SCR at 23 °C. The enzymatic assay for succinate–ubiquinone reductase (complex II)-catalyzed oxidation of succinate by 2,6-dichloroindophenol (DCIP) was carried out in essentially the same reaction mixture, except for the replacement of the oxidized cytochrome *c* with 53 μM DCIP. The reaction was initiated by the addition of enzyme and monitored continuously by following the absorbance change at certain wavelengths on a Perkin-Elmer Lambda 45 spectrophotometer equipped with a magnetic stirrer. The extinction coefficients used were 18.5 mM<sup>–1</sup> cm<sup>–1</sup> for A<sub>red-ox</sub><sup>550</sup> for cytochrome *c* reduction and 21 mM<sup>–1</sup> cm<sup>–1</sup> for A<sub>red-ox</sub><sup>600</sup> for DCIP reduction. For the inhibitory kinetic studies, the reaction was carried out in the presence of varying concentrations of the inhibitor.

The ubiquinol–cytochrome *c* reductase (*bc*<sub>1</sub> complex) activity in catalyzing the oxidation of DBH<sub>2</sub> by cytochrome *c* was assayed in 100 mM PBS (pH 6.5), 2 mM EDTA, 750 μM lauryl maltoside (*n*-dodecyl-β-D-maltoside), 20–115 μM DBH<sub>2</sub>, 100 μM oxidized

(37) Sheldrick, G. M. *SHELXTL*, Version 5.0; University of Göttingen: Göttingen, Germany, 2001.

## Scheme 3



cytochrome *c*, and an appropriate amount of SCR at 23 °C. The preparation of DBH<sub>2</sub> from DB was carried out according to the procedure described in previous publications,<sup>40,41</sup> and the concentration of DBH<sub>2</sub> was determined by measuring the absorbance difference between 288 and 320 nm using an extinction coefficient of 4.14 mM<sup>-1</sup>cm<sup>-1</sup> for the calculation.<sup>42,43</sup> The nonionic detergent lauryl maltoside was used to decrease the interfering nonenzymatic activity,<sup>42–45</sup> though it was expected to affect the  $K_m$  value of DBH<sub>2</sub> to *bc*<sub>1</sub> complex.<sup>45</sup> For each reaction, the nonenzymatic rate for cytochrome *c* reduction was followed for at least 100 s before enzyme was added to initiate the reaction.

The reaction mechanism could be considered as shown in Scheme 3, where *E*, *S*, and *I* represent enzyme, substrate, and inhibitor, respectively. According to the substrate reaction kinetic theory, the concentration of product formed at time *t* is calculated by<sup>46</sup>

$$[P] = v_s t + \frac{v_0 - v_s}{k_{\text{obs}}} (1 - e^{-k_{\text{obs}} t}) \quad (6)$$

where  $v_0$  and  $v_s$  are the initial and steady-state velocities of the reaction in the presence of inhibitor, and  $k_{\text{obs}}$  is the observed first-order rate constant:

$$k_{\text{obs}} = A[I]_0 + B$$

$$A = \frac{k_{+0}K_m + k'_{+0}[S]}{K_m + [S]}$$

$$B = \frac{k_{-0}K_m^* + k'_{-0}[S]}{K_m^* + [S]}$$

We have  $K_m$  and  $K_m^*$  as the Michaelis–Menten constants:

$$K_m = \frac{k_{-1} + k_2}{k_1}$$

$$K_m^* = \frac{k_{-1}^*}{k_1^*}$$

The slow, tight-binding inhibitors can also be classified as competitive, noncompetitive, and uncompetitive on the basis of similar considerations, as in the case of the classical inhibitors. Experimentally, the type of inhibition can be ascertained by studying the effect of [S] on the apparent rate constants *A* and *B*:

$$\text{Competitive: } A = \frac{k_{+0}K_m}{K_m + [S]}, \quad B = k_{-0} \quad (7)$$

$$\text{Noncompetitive: } A = k_{+0}, \quad B = k_{-0} \quad (8)$$

$$\text{Uncompetitive: } A = \frac{k'_{+0}[S]}{K_m + [S]}, \quad B = \frac{k'_{-0}[S]}{K_m^* + [S]} \quad (9)$$

## Results and Discussion

**Homology Modeling and Computational Prediction.** Because the  $K_i$  values of all compounds were tested on the basis of the porcine *bc*<sub>1</sub> complex in this work, we first used the crystal structure of bovine heart cytochrome *bc*<sub>1</sub> in complex with AZ (PDB entry 1SQB at resolution of 2.69 Å) as a template to establish the three-dimensional (3D) structural model of the porcine *bc*<sub>1</sub> complex. The sequence alignment between the porcine *bc*<sub>1</sub> complex and the same subunit of the template indicates that only 38 out of 379 residues were found to be different from each other, showing very high homology of the porcine *bc*<sub>1</sub> with the template. The 3D structural models for porcine *bc*<sub>1</sub> in complex with inhibitors were simulated by integrating homology modeling, molecular docking, and energy minimizations as described in the Materials and Methods. As shown in Figure 1A, the porcine *bc*<sub>1</sub> complex is a dimer and has *C*<sub>2</sub> symmetry. Each monomer contains one *bc*<sub>1</sub> subunit in which the Q<sub>0</sub> site is situated. This Q<sub>0</sub> site is located near the intermembrane space and partially interacts with the *b*<sub>L</sub> heme group. The (*E*)β-methoxy methyl acrylate group and the phenyl group of AZ are orientated at the deep bottom of the binding pocket. The (*E*)β-methoxy methyl acrylate group interacts with residues Phe128, Tyr131, Val132, Gly142, and Ala143 from helix C and helix cd1, and residues Glu271 and Tyr 273 from the *ef* loop. This headgroup of the inhibitor blocks the way to the *b*<sub>L</sub> heme group, with the shortest distances around 6 Å, while the distance from the carbonyl oxygen atom of this headgroup of the inhibitor to the heme iron is about 10.5 Å. The carbonyl oxygen atom of this headgroup also forms a hydrogen bond with the backbone –NH group of residue Glu271 from the *ef* loop, further stabilizing the orientation of the headgroup of the inhibitor inside the Q<sub>0</sub> binding pocket. The phenyl group of the inhibitor packs residues Gly142, Val145, Ile146, Pro270, Ile268, and Tyr278 through extensive hydrophobic interactions. Compared with the conformation of AZ in the crystal structure (blue in Figure 1B), the rmsd for its docked conformation (red in Figure 1B) is only 0.77 Å. In addition, the calculated binding free energies for KM, AZ, and PY are in good agreement with the corresponding experimental data (Table 1, see below), indicating that our computational protocol is reliable.

The above computational protocol was then used to predict the potency of the designed compounds. The calculated binding free energies ( $\Delta G_{\text{calcd}}$ ), summarized in Table 1, indicate that compounds **5a–d** should have a significantly higher inhibitory potency than AZ and KM. In addition, compounds **5a**, **5b**, and **5d** should have an inhibitory potency similar to that of PY, whereas compound **5c** should have an inhibitory potency higher than that of PY. An ideal computational protocol can be used to predict not only compounds with a higher activity but also compounds with a lower activity. Therefore, in order to validate the predictability of the computational protocol, some hydroxy-protected compounds **6a–d** were also predicted to have a lower potency due to the lack of the intramolecular hydrogen bond.

Table 1 also summarizes the  $K_i$  values against the porcine *bc*<sub>1</sub> complex for the inhibition by the synthesized compounds and also by the commercial compounds that were used as the

(38) SMART V5.628, SAINT V6.45, and SADABS; Bruker AXS Inc.: Madison, WI, 2001.

(39) Yu, L.; Yu, C. A. *J. Biol. Chem.* **1982**, *257*, 2016–2021.

(40) Rieske, J. S. *Methods Enzymol.* **1967**, *10*, 239–245.

(41) Luo, C.; Long, J.; Liu, J. *Clin. Chim. Acta* **2008**, *395*, 38–41.

(42) Fisher, N.; Bourges, I.; Hill, P.; Brasseur, G.; Meunier, B. *Eur. J. Biochem.* **2004**, *271*, 1292–1298.

(43) Fisher, N.; Brown, A. C.; Sexton, G.; Cook, A.; Windass, J.; Meunier, B. *Eur. J. Biochem.* **2004**, *271*, 2264–2271.

(44) Fisher, N.; Meunier, B. *Pest Manag. Sci.* **2005**, *61*, 973–978.

(45) Chretien, D.; Slama, A.; Brière, J.; Munnich, A.; Rötig, A.; Rustin, P. *Curr. Med. Chem.* **2004**, *11*, 233–239.

(46) Tsou, C. L. *Adv. Enzymol.* **1988**, *61*, 381–436.

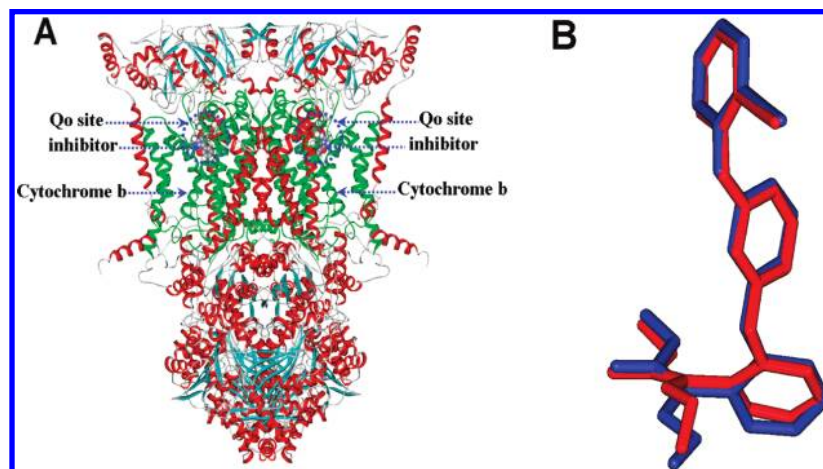
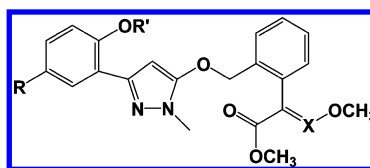


**Figure 1.** (A) Modeled 3D structure of porcine *bc*<sub>1</sub> complex with bound inhibitor. (B) Superimposition of the conformations of AZ in the crystal (blue) and modeled (red) structures.

**Table 1.**  $K_i$  Values of Compounds **5**, **6**, KM, AZ, and PY against Porcine *bc*<sub>1</sub> Complex



compd	R	R'	X	$K_i$ (nM)	$\Delta G$ (kcal/mol)		residue interaction energies (kcal/mol)	
					calcd <sup>a</sup>	exptl <sup>b</sup>	F274	P270
<b>5a</b>	H	H	CH	1.20	-11.11	-12.19	-10.55	-4.97
<b>5b</b>	CH <sub>3</sub>	H	CH	3.10	-11.40	-11.62	-10.24	-4.91
<b>5c</b>	Cl	H	CH	0.57	-12.50	-12.63	-10.28	-4.86
<b>5d</b>	H	H	N	3.80	-10.17	-11.50	-10.49	-4.88
<b>6a</b>	H	CH <sub>3</sub>	CH	29.10	-9.08	-10.29	-10.30	-4.95
<b>6b</b>	CH <sub>3</sub>	CH <sub>3</sub>	CH	19.90	-9.59	-10.52	-11.46	-5.06
<b>6c</b>	H	C <sub>6</sub> H <sub>5</sub> CH <sub>2</sub>	CH	12.70	-9.95	-10.79	-8.17	-4.70
<b>6d</b>	H	<i>p</i> -FC <sub>6</sub> H <sub>4</sub> CO	CH	97.70	-9.09	-9.56	-8.57	-4.95
AZ				297.60	-8.57	-8.92	-9.48	-4.53
KM				159.60	-8.90	-9.28	-9.13	-4.54
PY				3.30	-10.95	-11.59	-7.92	-6.23

<sup>a</sup>  $\Delta G_{\text{calcd}}$  was calculated according to our modified MM-PBSA method. <sup>b</sup>  $\Delta G_{\text{exptl}} = -RT \ln K_i$ .

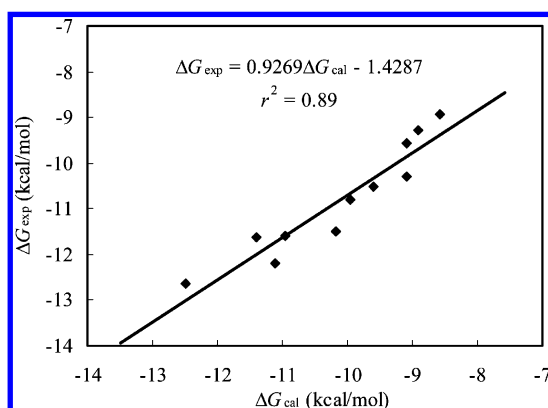


**Figure 2.** Correlation between the calculated and experimental binding free energies of compounds **5**, **6**, KM, AZ, and PY.

control. Interestingly, the calculated binding free energies correlated reasonably well with the binding free energies derived from the corresponding experimental  $K_i$  values, with a correlation coefficient of  $r^2 = 0.89$  (Figure 2), further confirming the reliability of our computational models. As shown in Table 1, compound **5c** distinguishes itself as the most promising candidate with the highest potency, with about 522-, 280-, and 5.8-

fold improved binding affinity compared to AZ, KM, and PY, respectively.

**Structural Basis of the Higher Binding Affinity of Compounds 5a–d.** As shown in Figure 3A,B, similar to that of AZ (Figure 3B), the methoxy methyl acrylate group of compounds **5a–5d** form a hydrogen bond with the backbone amide group of Glu271 (Figure 3A,B). However, compared to that of AZ (Figure 3C), the  $\pi$ - $\pi$  interactions between Phe274 and the pyrazole ring of compound **5** are improved greatly because the pyrazole ring and the 2-hydroxyphenyl are totally coplanar due to the intramolecular hydrogen bond between the hydroxyl group and the N(1) atom of pyrazole moiety (Figure 3D). In other words, compared with the conformation in the AZ-complexed *bc*<sub>1</sub>, the phenyl side chain of Phe274 undergoes a rotation of  $\sim 4^\circ$  in order to enhance the  $\pi$ - $\pi$  interactions with compound **5c**. Figure 3E shows the results of the superimposition of compounds **5a–d** based on the binding pocket. As a result, with about 522-, 280-, and 5.8-fold improvement of the binding affinity compared respectively with AZ, KM, and PY, compound **5c** is clearly the most potent inhibitor. In contrast, the hydroxy-protected derivatives **6a–d** all have a lower binding affinity due to the lack of such an intramolecular hydrogen bond.

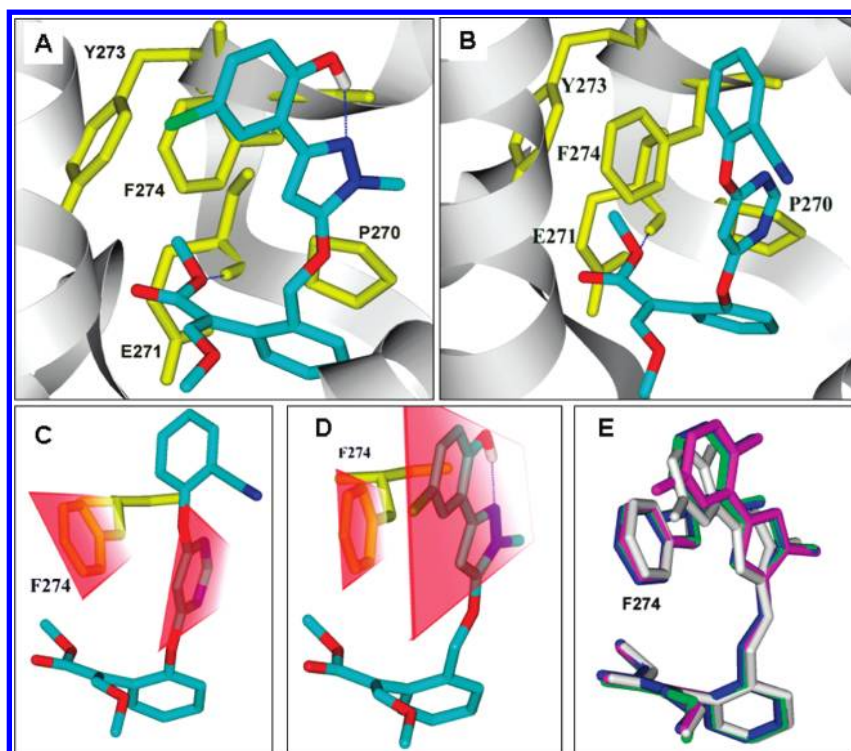
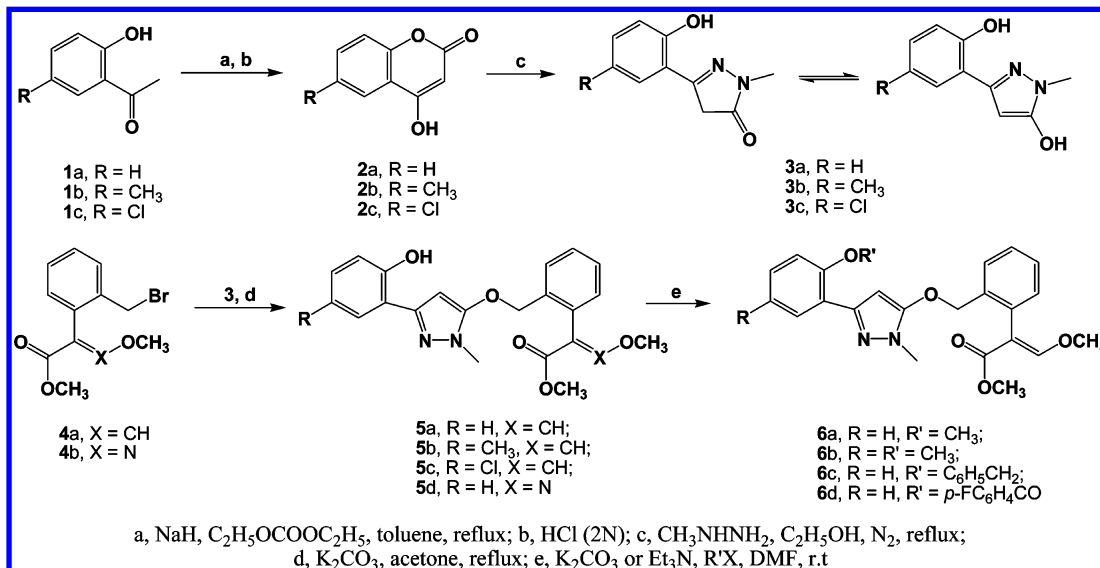


**Figure 3.** Comparison of the binding modes of compound **5c** and AZ. (A) Simulated binding model of *bc1* in complex with **5c**. (B) Simulated binding model of *bc1* in complex with AZ. (C)  $\pi$ - $\pi$  stacking interaction between the side chain of F274 and the pyrimidyl ring of AZ (the interaction energy between F274 and AZ is  $-9.48$  kcal/mol). (D)  $\pi$ - $\pi$  stacking interaction between the side chain of F274 and the enlarged aromatic system of **5c** (the interaction energy between F274 and **5c** is  $-10.28$  kcal/mol). (E) Superimposition of the binding conformation of compounds **5a** (green), **5b** (white), **5c** (magenta), and **5d** (blue).

#### Scheme 4



**Synthesis of the Designed Compounds.** The synthetic route for the designed compounds **5** and **6** is shown in Scheme 4. 4-Hydroxy-2*H*-chromen-2-one (also named 4-hydroxycoumarin) compounds **2** were prepared easily from 2'-hydroxyacetophenones **1a–c** as starting material in good overall yields (85% for **2a**, 72% for **2b**, and 75% for **2c**). Compounds **2** were then reacted with methylhydrazine to afford the key intermediates **3a–c**, which are 3-(2-hydroxyphenyl)-1-methyl-1*H*-pyrazol-5(4*H*)-ones. It should be noted that compounds **3** underwent tautomerization under basic conditions to produce the enol isomers. Fortunately, maybe due to the existence of an intramo-

lecular hydrogen bond, the resulted enol-hydroxy was apparently more active than the phenol-hydroxy group and reacted with (*E*)-methyl 2-(2-bromomethyl-phenyl)-3-methoxyacrylates **4** under basic conditions to produce the target compounds **5** in yields of 67–84%. In addition, in order to examine the importance of the intramolecular hydrogen bond, we also synthesized some hydroxy-protected compounds **6a–d** by the reactions of compounds **5a** and **5b** with various alkylation or acetylation reagents. The structures of compounds **2–6** were characterized by <sup>1</sup>H NMR, EI-MS spectrum, and elemental analyses. In addition, the crystal structure (CCDC 709734) of

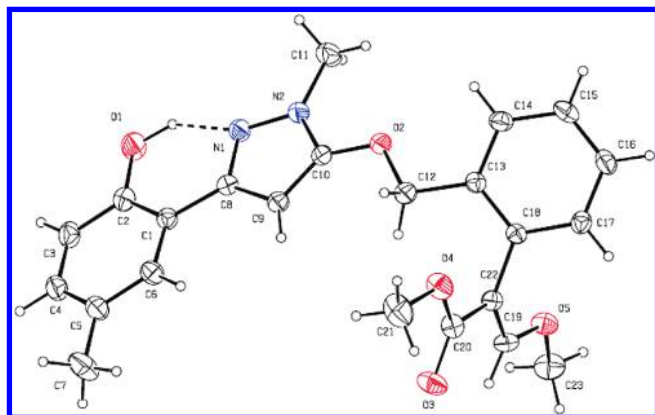


**Figure 4.** Crystal structure of compound **5b**. The dotted line shows the intramolecular H-bond.

**5b** was determined by X-ray diffraction analyses. As shown in Figure 4, the  $\beta$ -methoxyacrylate group adopts *E*-configuration. Most interestingly, an intramolecular hydrogen bond between the hydroxyl group and the N(1) atom was formed, as expected. As a result, the pyrazole ring and the 2-hydroxyphenyl planes are coplanar to form a bigger aromatic system.

**Enzymatic Kinetics.** In order to understand the action mechanism, we further studied the inhibitory kinetics of succinate-cytochrome *c* reductase (SCR, mixture of respiratory complex II and *bc*<sub>1</sub> complex) with compounds **5a–d**. Complex II first passes electrons from succinate to ubiquinone, and then the cytochrome *bc*<sub>1</sub> complex passes electrons from reduced ubiquinone to cytochrome *c*. We measured the succinate-ubiquinone reductase (complex II) activity of SCR using succinate and DCIP as substrates and the succinate-cytochrome *c* reductase (both complex II and *bc*<sub>1</sub> complex) activity of SCR using succinate and cytochrome *c* as substrates. All of the compounds exhibited no effect on the activity of complex II (data not shown), whereas they inhibited the activity of succinate-cytochrome *c* reductase considerably (Figure 5). Thus, the inhibition of these compounds on the activity of SCR may be attributed to their effects on the function of *bc*<sub>1</sub> complex, and the assay for the SCR-catalyzed oxidation of succinate by cytochrome *c* was used to elucidate the inhibitory kinetics of the *bc*<sub>1</sub> complex. As is the case for many slow-binding inhibitors, the progress curves in the presence of compounds **5a–d** did not display a simple linear product versus time relationship, as seen for classical reversible inhibitors like AZ and KM. Rather, the product formation versus time shows a curvilinear function. For example, Figure 5A shows the time courses of the *bc*<sub>1</sub> complex-catalyzed reaction in the presence of different concentrations of compound **5c**. The progress curves start off linear (the initial-rate phase) but fall off with increasing time. When time (*t*) approaches infinity, the concentration of product ([P]) approaches an asymptote with a positive slope, which decreases with increasing concentration of compound **5c**. The initial-rate phase reflects the slow onset of inhibition by these compounds, since it can be simply eliminated by preincubating the inhibitor with the enzyme (data not shown). Under the conditions employed in the present study, the time-dependent behavior of the enzyme-catalyzed reaction can be well described according to the substrate reaction kinetic theory.<sup>46</sup> The best-fit curves in Figure 5A were obtained by nonlinear regression analysis, from which the kinetic parameters, the initial ( $v_0$ ) and steady-state ( $v_s$ ) velocities of the reaction in the presence of inhibitor,

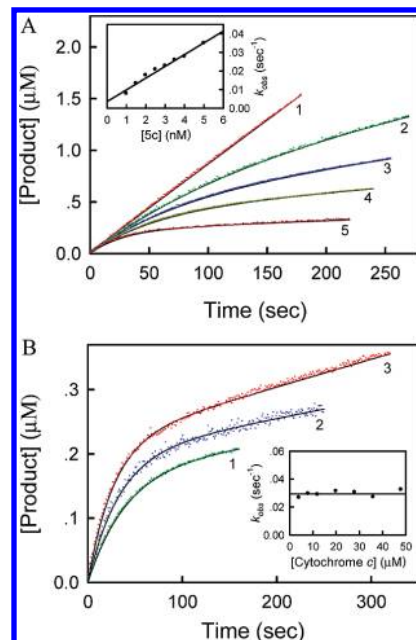


**Figure 5.** (A) Inhibitory kinetics of *bc*<sub>1</sub> complex by compound **5c**. Each reaction mixture contains 100 mM PBS (pH 7.4), 0.3 mM EDTA, 20 mM succinate, 60  $\mu$ M cytochrome *c*, 0.1 nM SCR, and a certain amount of compound **5c** (1, 0 nM; 2, 1 nM; 3, 1.5 nM; 4, 2 nM; and 5, 5 nM). Experimental data are shown as colored dots and theoretical values as black solid lines. Inset: Plot of  $k_{\text{obs}}$  against concentration of compound **5c**. (B) Effect of cytochrome *c* concentration on the inhibition of *bc*<sub>1</sub> complex by compound **5c**. The assays were carried out in the presence of 5 nM compound **5c** and various concentrations of cytochrome *c* (1, 4  $\mu$ M; 2, 12  $\mu$ M; and 3, 48  $\mu$ M). Each reaction was initiated by adding 0.1 nM SCR. Inset: Plot of  $k_{\text{obs}}$  against concentration of cytochrome *c*.

and the observed first-order rate constant ( $k_{\text{obs}}$ ) can be determined. The inset of Figure 5A shows the plot of  $k_{\text{obs}}$  against the concentration of compound **5c** ( $[5c]$ ). Noticeably,  $k_{\text{obs}}$  is proportional to the inhibitor concentration. From the slope and intercept of this plot, the apparent rate constants  $A = 0.00631 \pm 0.00036 \text{ s}^{-1} \text{ nM}^{-1}$  and  $B = 0.00358 \pm 0.00110 \text{ s}^{-1}$  were then determined.

Subsequently, we monitored the time courses of the *bc*<sub>1</sub> complex-catalyzed reaction in the presence of different concentrations of cytochrome *c* and at a fixed concentration of compound **5c** (Figure 5B). Using the procedures described above, the values of  $k_{\text{obs}}$  can be obtained by fitting the progress curves according to the substrate reaction kinetic theory and are plotted against the concentration of cytochrome *c* in the inset of Figure 5B. The data clearly revealed that  $k_{\text{obs}}$  was independent of the concentration of substrate cytochrome *c* under the experimental conditions used, indicating that compound **5c** is a noncompetitive inhibitor with respect to cytochrome *c*. Thus, the values of *A* and *B* determined from Figure 5A are equal to the true association and dissociation rate constants  $k_{+0}$  and  $k_{-0}$ , respectively, and the inhibition constant for compound **5c** can be calculated as  $K_i = k_{-0}/k_{+0} = 0.57 \pm 0.21 \text{ nM}$ .

To study the effect of substrate ubiquinol on the inhibition kinetics of compound **5c**, we directly measured the ubiquinol-cytochrome *c* reductase (*bc*<sub>1</sub> complex) activity of SCR using decylubiquinol (DBH<sub>2</sub>) and cytochrome *c* as substrates in the absence and in the presence of compound **5c**. This reaction exhibited Michaelis–Menten kinetics toward substrate DBH<sub>2</sub>, and the kinetic parameters were determined ( $K_m = 58 \pm 4 \mu\text{M}$  and  $k_{\text{cat}} = 238 \pm 8 \text{ s}^{-1}$ ). In the presence of compound **5c**, with succinate used as substrate, the progress curves exhibited a similar curvilinear

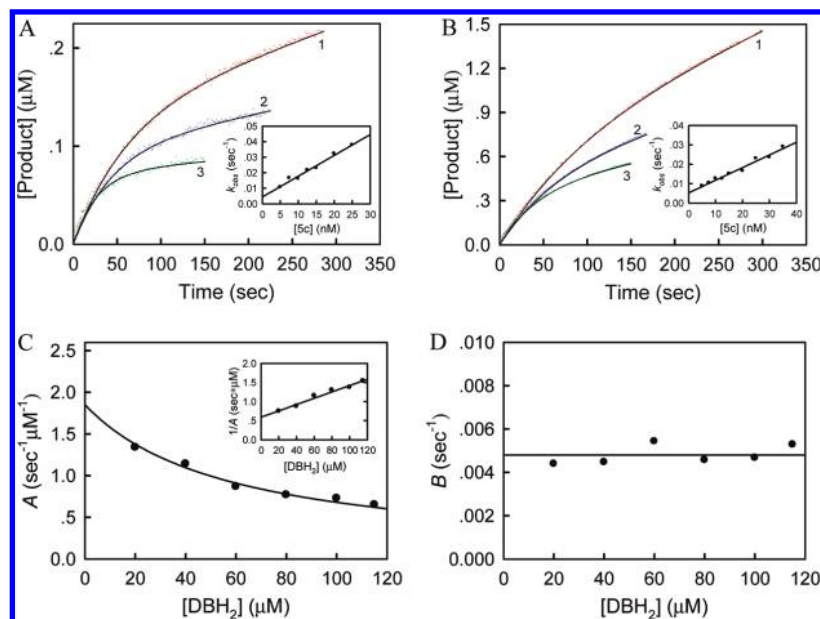


**Figure 6.** (A,B) Inhibitory kinetics of porcine *bc*<sub>1</sub> complex by compound **5c**. Each reaction mixture contains 100 mM PBS (pH 6.5), 2 mM EDTA, 750  $\mu$ M lauryl maltoside, 100  $\mu$ M oxidized cytochrome *c*, 0.05 nM SCR, a certain amount of DBH<sub>2</sub> (A, 20  $\mu$ M; B, 115  $\mu$ M), and compound **5c** (1, 7.5 nM; 2, 15 nM; and 3, 25 nM). Experimental data are shown as colored dots and theoretical values as black solid lines. Insets: Plots of  $k_{\text{obs}}$  against concentration of compound **5c**. (C) Plot of the apparent rate constant *A* against concentration of DBH<sub>2</sub>. Inset: Plot of  $1/A$  against concentration of DBH<sub>2</sub>. (D) Plot of the apparent rate constant *B* against concentration of DBH<sub>2</sub>.

pattern due to the slow onset of inhibition (Figure 6). However, when the experiments were performed at a fixed concentration of compound **5c**, the  $k_{\text{obs}}$  value decreased with increasing concentration of DBH<sub>2</sub> (Supporting Information, Figure 2s), which is different from what is observed in Figure 5B. To further elucidate the inhibitory mechanism, we carried out six sets of inhibitory experiments in the presence of varying concentrations of DBH<sub>2</sub> and compound **5c** (Figure 6A,B). Similarly, from these progress curves of product formation at fixed concentrations of DBH<sub>2</sub>, the values of  $v_0$ ,  $v_s$ , and  $k_{\text{obs}}$  can be determined as described previously. Plots of  $k_{\text{obs}}$  against the inhibitor concentration give a straight line (insets of Figure 6A,B), from which the values of *A* (slope) and *B* (intercept) at indicated DBH<sub>2</sub> concentrations were obtained. Figure 6C,D shows the dependence of the *A* and *B* values on the DBH<sub>2</sub> concentration. Clearly, *A* decreased with increasing the concentration of DBH<sub>2</sub>, while *B* was not affected, suggesting that compound **5c** is a competitive inhibitor with respect to substrate ubiquinol. Thus, with the  $K_m$  value of 58  $\mu$ M, the microscopic inhibition rate constants  $k_{+0} = 0.00185 \pm 0.00003 \text{ s}^{-1} \text{ nM}^{-1}$  and  $k_{-0} = 0.00480 \pm 0.00018 \text{ s}^{-1}$  can be obtained by fitting eq 2 to the experimental data, and the inhibition constant  $K_i = k_{-0}/k_{+0} = 2.6 \pm 0.1 \text{ nM}$  can be derived. The  $K_i$  value determined is about 5-fold higher than that measured from the succinate-cytochrome *c* reductase activity inhibition, which is mainly due to the presence of lauryl maltoside. This nonionic detergent was reported to affect the  $K_m$  value of DBH<sub>2</sub> to *bc*<sub>1</sub> complex,<sup>45</sup> and it possibly has an impact on the microscopic inhibition rate constants and the  $K_i$  value. Indeed, we found that the  $k_{\text{obs}}$  value decreased with increasing concentration of lauryl maltoside at fixed DBH<sub>2</sub> and compound **5c** concentrations (Supporting Information, Figure 3s).

## Conclusion

In summary, we have successfully designed and synthesized a series of pyrazole derivatives as inhibitors of cytochrome *bc*<sub>1</sub>

complex. By introducing an intramolecular hydrogen bond to form a big aromatic system, the  $\pi$ - $\pi$  interactions with the phenyl of Phe274, an important residue with conformational flexibility located in the binding pocket, were significantly improved. As a result, a new *bc*<sub>1</sub> inhibitor with subnanomolar  $K_i$  potency was discovered. Compound **5c**, with a  $K_i$  value of 570 pM, was found to display about 522-, 280-, and 5.8-fold improved binding affinity compared to the commercial inhibitors AZ, KM, and PY, respectively. The further inhibitory kinetics studies showed that compound **5c** is a noncompetitive inhibitor with respect to substrate cytochrome *c* but a competitive inhibitor with respect to substrate ubiquinol. Due to its subnanomolar  $K_i$  potency and slow dissociation rate ( $k_{-0} = 0.00358 \text{ s}^{-1}$ ), compound **5c** could be used as a specific probe for further elucidating the mechanism of *bc*<sub>1</sub> function and as a new lead compound for future drug discovery. In addition, the present work provides a successful case study concerning how to improve binding affinity of a ligand with a receptor by optimizing the interactions of the ligand with conformationally flexible residues of the receptor.

**Acknowledgment.** The research was supported in part by the National Basic Research Program of China (No. 2010CB126103), the NSFC (No. 20925206, 20932005, and 20872045), and the NIH (RC1MH088480). The authors also acknowledge Dr. Z. X. Wang for critical discussions and reading of the manuscript.

**Supporting Information Available:** Complete refs 8 and 20; Figure 1s, sequence alignment of the Q<sub>0</sub> pocket residue; Figure 2s, inhibitory kinetics of porcine *bc*<sub>1</sub> complex by compound **5c**; Figure 3s, effect of lauryl maltoside on  $k_{\text{obs}}$ ; and Figure 4s, enzyme kinetics of AZ. This material is available free of charge via the Internet at <http://pubs.acs.org>.

JA905756C